Fine-Scale Electric Fields and Joule Heating From Observations of the Aurora

P. Krcelic[1] [ID], **R. C. Fear[1]** [ID], **D. Whiter[1]** [ID], **B. Lanchester[1]** [ID], **A. L. Aruliah[2]** [ID], **M. Lester[3]** [ID], and **L. Paxton[4]** [ID]

[1]Physics and Astronomy, University of Southampton, Southampton, UK, [2]Atmospheric Physics Laboratory, University College London, London, UK, [3]University of Leicester, Leicester, UK, [4]Applied Physics Laboratory, Johns Hopkins University, Laurel, MD, USA

Abstract Optical measurements from three selected wavelengths have been combined with modeling of emissions from an auroral event to estimate the magnitude and direction of small-scale electric fields on either side of an auroral arc. The temporal resolution of the estimates is 0.1 s, which is much higher resolution than measurements from Super Dual Auroral Radar Network (SuperDARN) in the same region, with which we compare our estimates. Additionally, we have used the Scanning Doppler Imager instrument to measure the neutral wind during the event in order to calculate the height integrated Joule heating. Joule heating obtained from the small scale electric fields gives larger values (17 ± 11 and 6 ± 9 mWm^{-2} on average on each side of the arc) than the Joule heating obtained from more conventionally used SuperDARN data (5 mWm^{-2}). This result is significant, because Joule heating will cause changes in the thermosphere from thermal expansion and thermal conductivity, and may also affect the acceleration of the neutral wind. Our result indicates that high spatial and temporal resolution electric fields may play an important role in the dynamics of the magnetosphere-ionosphere-thermosphere system.

1. Introduction

Magnetosphere-ionosphere interactions play a major role in the dynamics of near Earth space which also impact the atmosphere and surface infrastructure. Auroral electric fields are an important link in the magnetosphere-ionosphere interaction, causing Joule heating in the ionosphere (B. S. Lanchester et al., 1996), thus acting as a major source of atmospheric dynamics (>100 km altitude). Ionospheric feedback also occurs, where the ionosphere plays a significant role in auroral dynamics (Russell et al., 2013). Measurements of auroral electric fields have been conducted using rocket and satellite measurements (Marklund et al., 1994), incoherent scatter radar measurements (Aikio et al., 2002; B. S. Lanchester et al., 1997), coherent scatter radars (Chisham et al., 2007), optical measurements (Dahlgren et al., 2016; Tuttle et al., 2014), or with the combination of two or more measurement techniques, such as a combination of rocket measurements and ground auroral imagery (Clayton et al., 2019). The biggest drawback with direct rocket and satellite measurements is the rapid movement of the instrument, resulting in good spatial coverage but poor temporal coverage. Radar measurements are reliable but have poor spatial and temporal resolution for small-scale electrodynamics. Measured small scale electric fields plus measured local neutral wind can be used to estimate Joule heating (e.g., Billett et al., 2018). Aruliah et al. (2005) investigated Joule heating using 1-min versus 15-min average European incoherent scatter radar (EISCAT) velocities for a common volume tristatic FPI-EISCAT experiment, together with the full neutral wind vector obtained from 3 Fabry−Perot interferometers at Sodankylä, Kiruna and Skibotn. These heating estimates are usually underestimated and a possible explanation for such underestimates could be the highly variable nature of ionospheric electric fields, which is usually missed with radar observations (Deng & Ridley, 2007). The rapid development of technology and modeling techniques in the last decades has resulted in more accurate and more numerous optical studies of the aurora. Dahlgren et al. (2009) first estimated local drift velocities observing afterglow, by combining images of the 732 nm emission, with modeling techniques. Auroral emission from O$^+$ (^{2}D-^{2}P) at 732.0 nm has a lifetime of approximately 5 s, and therefore by combining images of this emission with modeling and images of different prompt emissions, it is possible to determine the O$^+$ ion velocity and hence electric field. Tuttle et al. (2020) expanded the technique and applied it to observations of a single arc structure.

In the present paper we have further expanded the technique of Tuttle et al. (2020) and Dahlgren et al. (2009) to estimate the small-scale electric fields on either side of an auroral arc. Time resolution is 0.1 s, while the spatial

resolution depends on the size of the feature being tracked, which is 1–2 km on each side of the arc. The distance between the two features is less than 2 km through the event. Furthermore, we have used the measured electric fields to estimate the local height integrated Joule heating at subsecond resolution.

2. Instruments

2.1. ASK

The Auroral Structure and Kinetics instrument (ASK) is a multimonochromatic imager designed to measure fine-scale structures of the aurora. ASK consists of three cameras observing the magnetic zenith, each with a different narrowband filter centered around a selected wavelength (B. Lanchester & Gustavsson, 2012). The cameras are labeled as ASK1, ASK2, and ASK3, and are time synchronized. Each camera uses an electron-multiplying charge-coupled device (EMCCD) detector, with 512×512 pixels, binned to 256×256 to increase the readout speed. An EMCCD is a photosensitive chip which incorporates electron multiplying in order to amplify weak or single photon events above the read noise. The optical setting is equipped with f/1 lenses with a focal length of 75 mm, resulting in a $6.2° \times 6.2°$ field of view. Galilean-type converters can be applied to achieve a $3.1° \times 3.1°$ field of view. In the present event the second camera (ASK2) was observing emission from a higher altitude than the other two cameras, so it was equipped with a converter to reduce the field of view, thereby observing the same field lines as ASK1 and ASK3 without converters. During the event studied in this work, the instrument was observing at a cadence of 20 Hz.

2.1.1. ASK1—673 nm

ASK1 has a filter centered on 673 nm with a passband of 14 nm, observing the N_2 1PG (first positive group) (5,2) and (4,1) band emissions, with peak emission varying between 100 and 200 km, resulting from the excitation of the N_2 molecules by the precipitating electrons (Ashrafi et al., 2009). The N_2 1PG emissions show little to no dependence on the energy of the precipitating electrons. N_2 emissions are used to estimate the flux of precipitating electrons by dividing the emission in Rayleighs by a coefficient dependent on the precipitating electron energy distribution for the event, as explained in B. S. Lanchester et al. (2009). There are no other emissions contaminating the ASK1 channel.

2.1.2. ASK2—732 nm

ASK2 observes emissions from the metastable $O^+(^2P)$ ion with a 1 nm passband centered on 732 nm. Oxygen ions are produced by electron precipitation. Rees et al. (1982) showed that 18% of the total O^+ ionization results in the $O^+(^2P)$ state, which is further divided into two levels of different total angular momentum: the $^2P_{1/2}$ and $^2P_{3/2}$. In total there are 4 transitions, $(^2P_{1/2,3/2} \rightarrow {}^2D_{3/2,5/2})$, which form two doublets (centered on 732 and 733 nm), from which we observe only one doublet with $^2D_{5/2}$ as the lower state. $O^+(^2P)$ states are metastable with a lifetime of ≈5 s, which allows the auroral features to be tracked and thus estimate the local electric fields (Dahlgren et al., 2009). The peak emission height of metastable $O^+(^2P)$ ions is around 250 km. The ASK2 channel is contaminated by OH airglow and the (5,3) band of the N_2 1PG band system. OH airglow decontamination is achieved by background correction, while for the N_2 1PG decontamination we use the method described in Spry et al. (2014), where we subtract 2.5% of the ASK1 image brightness from the ASK2 image.

2.1.3. ASK3—777 nm

ASK3 observes emissions caused by a transition between the atomic oxygen ^5P and ^5S states. The peak emission of this transition is broad and highly dependent on the energy of precipitating electrons, due to it being produced by the two competing processes: dissipation of molecular oxygen and excitation of atomic oxygen. The ASK3 filter is centered on 777.4 nm and has a passband of 1.5 nm (B. S. Lanchester et al., 2009). The 777.4 nm emissions are highly dependent on the energy of the precipitating electrons. Therefore, the ratio between ASK1 and ASK3 brightness can be used to estimate the precipitating electron energy as described in B. S. Lanchester et al. (2009). There are no other emissions contaminating the ASK3 channel.

2.2. SuperDARN

The Super Dual Auroral Radar Network (SuperDARN) is a network of coherent scatter radars observing the polar cap regions (Chisham et al., 2007). Each radar scans with 16–20 beams with each beam scan taking from 3 to

6 s, thus resulting in a full radar sweep typically taking 1 or 2 min. SuperDARN operates in the high-frequency range and uses the Doppler shift of radar pulses which are reflected from decameter-scale irregularities in the ionosphere at ≈250 km altitude to obtain the line-of-sight (LOS) ion velocities. In this study, we obtain 2D horizontal convection velocities from a fitting process which constructs potential maps using all radar measurements in a single radar sweep (Ruohoniemi & Greenwald, 1996). Each individual SuperDARN radar makes observations with a range resolution of typically 45 km, although 15 km resolution can be achieved. The map potential technique introduced by Ruohoniemi and Greenwald (1996) further increases the spatial resolution to of order 100 km. These are much greater than the spatial resolution being investigated here. The purpose of using Super-DARN here is to provide an independent estimate of the convection electric field on the larger scale size that is often used in numerical simulations of the high latitude ionosphere.

2.3. SCANDI

In order to measure the neutral wind velocities we use the Scanning Doppler Imager (SCANDI) located on Svalbard (Aruliah et al., 2010). SCANDI observes an area with 500 km radius over Svalbard, by dividing it into zones in a way which forms multiple concentric rings. LOS neutral wind velocities are measured in each zone using the Doppler shifts of the 630 nm emission from airglow and aurora. The height of peak 630 nm emission, and thus the neutral wind measurements, is 240–250 km. An averaged 2D neutral wind can be obtained from the LOS velocities in each ring of the imaging area. A full sweep of the SCANDI instrument takes around 7.5 min.

3. Method

3.1. Modeling of Metastable Emissions

The method of Tuttle et al. (2020) has been used in the present work to model the auroral emissions. Full details can be found in that paper, but a brief description is provided here. Prior to the analysis, the magnetic zenith needs to be estimated. This is easily done if auroral rays are present in the event. The orientation of the rays and their intersection are then used to give the position of the magnetic zenith. Auroral rays were present a few seconds before the event and we used the same zenith estimation technique as used in Tuttle et al. (2020). The model is then applied on a 3D grid with dimensions 30 km × 30 km × 410 km. The spatial resolution (both horizontal and vertical) is set to 200 m and the volume is oriented such that the long axis lies along the magnetic field lines, and horizontal axes are oriented to match the camera orientation. Final results are then oriented to a N-E coordinate system. The process to fill the volume is performed using the following steps. First, the peak energy of precipitating electrons at each pixel is determined using the ratio of the emissions from the images of ASK1 and ASK3 (the two cameras observing prompt emissions). The Southampton ion chemistry model is used (B. S. Lanchester et al., 2009), which gives 1D profiles of densities, production and emission of the major species in the Earth's high altitude atmosphere, with input of the precipitating electron energy distribution, ap and f10.7 indices. A set of profiles is produced by varying the peak energy of the precipitating electron population, but assuming the energy distribution is Gaussian in shape. Each pixel is assigned to a corresponding profile. We then search for the column of a 3D volume where the field of view of a pixel intersects the height of the peak emission from the N_2 1PG profile of a given pixel. The emission profile is then assigned to a given column in a 3D space. This process is done for each pixel in the image in order to fill a 3D volume. For ASK1 and ASK3 the volume is populated with the N_2 1PG and atomic oxygen emissions from the ion chemistry model.

For metastable emissions of ASK2 the volume is filled with the O^+2P production rates since in order to calculate the emissions we need to include the horizontal drift velocities in our model. The $O^+(2P)$ emission is proportional to the O^+ density distribution with the continuity equation:

$$\frac{dn}{dt} = q - \sum_k \alpha_k n_k n - \sum_j A_j n - \nabla \cdot (n\vec{V}),$$ (1)

where n is the density of the $O^+(^2P)$ ions, q is the production rate of the species, A_j represent the Einstein coefficients, α represent the quenching rates, n_k are the densities of the quenching species k, and $\vec{V}$ is a drift velocity. Production rates are obtained from the ion chemistry model as outlined above (B. S. Lanchester et al., 2009). The second and third terms on the right hand side of the equation are loss processes due to the quenching and the emissions. Particles are quenched in collisions with other species. Therefore quenching is greater at regions of increased density (lower altitudes). O^+ is quenched by the electrons, atomic oxygen and molecular
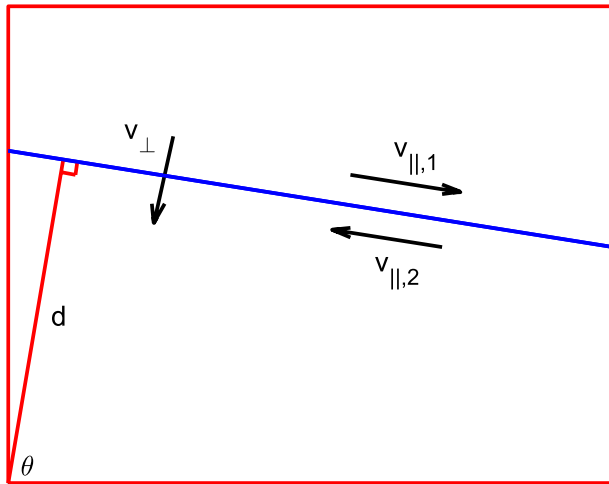
Figure 1. Schematic representation of model parameters, from top view of tomographic volume. The blue line represents the separatrix, while black vectors represent velocities. θ, d are separatrix parameters and, $v_\perp$, $v_{\|,1}$, $v_{\|,2}$ are given velocities.

nitrogen. Quenching rates for each species have been studied in detail (Chang et al., 1993; Rees, 1989; Stephan et al., 2003). The third term corresponds to the loss due to emission, which is when a particle de-excites and releases a photon. Einstein emission coefficients are obtained from Zeippen (1987). The 732 nm emission line has contributions from $J_{1/2}$ and $J_{3/2}$ upper states, which means that Equation 1 must be solved for each state. Since the South-ampton ion chemistry model gives the production of a whole $O^+(^2P)$ ion species, we use the ratio $n_{1/2}/n_{3/2} = 0.367$ given in Whiter et al. (2014) to separate the two states. The continuity equation is solved using the method described in Gustavsson et al. (2001). Modeled images are formed from the O^+ density and Einstein coefficients using the blob-based projection method of Rydesäter and Gustavsson (2000).

The drift velocity in Equation 1 is treated as a free parameter, which we solve, by minimizing the error:

$$err(V) = \sum_{u,v} [I_{obs}(u,v) - I_{mod}(u,v,n(V))]^2. \tag{2}$$

$I_{obs}(u,v)$ is the observed intensity at pixel (u,v), where u and v are coordinates of the pixel. $I_{mod}(u,v,n(V))$ is the modeled intensity at pixel (u,v) from the camera field of view for a given O^+ density $n(V)$ which is a function of a free velocity parameter V. We calculate χ^2 values in the same manner, with the assumption that each pixel (measurement) has the same variance. From χ^2 values we are able to calculate confidence intervals and therefore the standard deviations of free parameters. From the estimated drift velocities and the local magnetic field, obtained from the IGRF11 model (Finlay et al., 2010), the electric fields are calculated using the following equation:

$$\vec{E} = -\vec{V} \times \vec{B} \tag{3}$$

where $\vec{E}$ represents the electric field, $\vec{B}$ is the magnetic field and $\vec{V}$ is drift velocity. The described method requires some assumptions which are potential source of the uncertainty (e.g., zenith position estimation, precip-itating electron distribution, camera noise). Therefore we have made a rigorous error analysis on synthetically generated data to verify our method. The results of the error analysis are presented in Supporting Information S1 material of this paper.

3.2. Double Flow

The above method assumes that there is only one velocity across the field of view of the cameras, whereas observations and theory suggest that the electric field is much more complex in the presence of auroral arcs. The logical next step is therefore to divide the tomographic 3D volume into two parts with different drift velocities. The region dividing the two volumes is called the separatrix and is defined with two parameters, angle θ and distance d from the reference point in a tomographic reference plane. Figure 1 shows a schematic representation of the parameters from the view perpendicular to the magnetic field lines. We are assuming that the drift veloc-ities have a common component ($v_\perp$) across the arc, and different components ($v_{\|,1}$, $v_{\|,2}$) along the arc. Such a setup has 5 free parameters: θ, d, $v_\perp$, $v_{\|,1}$, and $v_{\|,2}$. In order to reduce the number of parameters and in turn the computing time, we are determining the separatrix parameters (θ, d) using the height integrated $O^{+2}P$ production rates. From such images we are able to separate the different auroral structures. The separatrix is determined for each time step, and our model is effectively reduced to only three free parameters.

3.3. Joule Heating Estimation

One of the main goals of the research is to estimate the Joule heating profile, but for that we need the height profiles of both the neutral wind velocity and Pedersen conductivities. Obtaining such profiles is challenging, and therefore we make the following simplifying assumptions. We calculate the height integrated Joule heating ($\sum Q_J$) and the height integrated Pedersen conductivity ($\sum \sigma_P$). It should be noted, that we did not do the height integration but used the empirical formula for height integrated Pedersen conductivity, which assumes integration over the whole column. The electric fields obtained from modeling of the $O^+(^2P)$ ions are assumed to be constant across
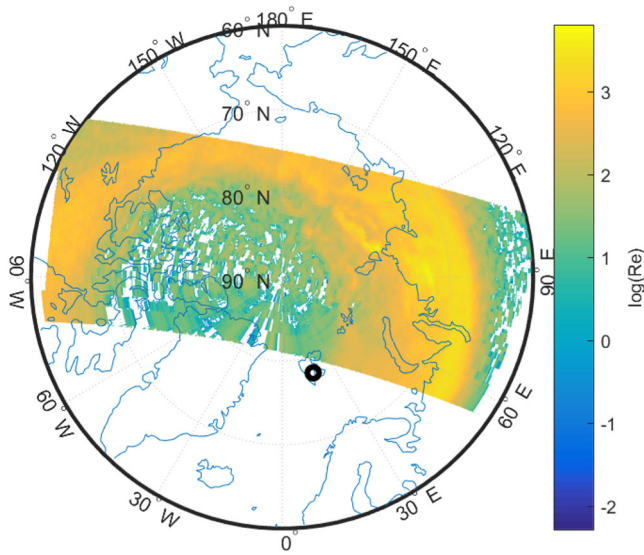
Figure 2. Auroral LBH-S emission seen from Defense Meteorological Satellite Program F16 spacecraft cut in time between 23:15:18 and 23:31:25 UT on 21 December 2014. Results are given in geographical coordinates and the location of Svalbard is indicated with a black circle.

the height profile due to the assumption of straight, non-diverging magnetic field lines in the area of observation. We also assume that the average neutral wind ($\vec{v_N}$) is represented by the neutral wind measurements obtained from the SCANDI instrument. This is a weak assumption since neutral wind changes significantly with height, but as is shown below, neutral wind plays a minor role in local Joule heating close to auroral structure where there are large and highly variable electric fields. In order to estimate a height integrated Joule heating we use equation (e.g., Baker et al., 2004; Billett et al., 2018):

$$\sum Q_J = \sum \sigma_P E^2 + 2 \sum \sigma_P \vec{E} \cdot \left(\vec{v_N} \times \vec{B} \right) + \sum \sigma_P \left(\vec{v_N} \times \vec{B} \right)^2, \quad (4)$$

where $\sum Q_J$ represents the height integrated Joule heating, $\sum \sigma_P$ height integrated Pedersen conductivity, and $\vec{v_N}$ neutral wind velocity. $\vec{E}$ and $\vec{B}$ are the electric and magnetic fields respectively. The height integrated Pedersen conductivity is estimated using the equations for solar Pedersen conductivity from Rich et al. (1987) and auroral Pedersen conductivity from Robinson et al. (1987). The total Pedersen conductivity is calculated as:

$$\sum \sigma_P = \sqrt{\sum \sigma_{P,A}^2 + \sum \sigma_{P,S}^2}, \quad (5)$$

where $\sum \sigma_{P,A}^2$ and $\sum \sigma_{P,S}^2$ are auroral and solar Pedersen conductivities respectively.

4. Data and Results

For our analysis we are using an event from 21 December 2014. We have analyzed 4 s of the increased auroral dynamics centered around the time 22:47:45 UT. During this event interplanetry magnetic field (IMF) B_z was positive and had a value of 3.25 nT, IMF B_y was 10.52 nT and auroral electrojet index was 444 nT.

Figure 2 shows the Defense Meteorological Satellite Program F16 satellite image of the aurora from observations of Special Sensor Ultraviolet Spectrographic Imager (SSUSI) Lyman-Birge-Hopfield-short (LBH-S) emission. Although the satellite image does not cover Svalbard, the F16 image is the closest available both temporally and spatially to our event. From the location of the auroral zone seen in Figure 2, and the fact that we have observed an auroral arc over Svalbard, we can claim with confidence that Svalbard was at the poleward edge of the auroral zone at the time of our observation. The SSUSI images show blurred aurora, while the ASK images show a clear and sharp arc. The reason for this difference lays in both the temporal and spatial resolutions of the two instruments. Since SSUSI images a wider area and samples over a longer time period, rapidly moving small scale auroral features seem blurred, while ASK can clearly distinguish such features.

Figure 3 shows the time evolution of our event seen from all three ASK cameras. The black squares on the images for the two prompt emissions (ASK1 and ASK3) represent the field of view of the ASK2 camera. The time evolution of the metastable emissions during the event can be seen in the second row of Figure 3. Note that the X-axis is inverted to give a view from above, so that the results can be compared more easily with the geographic coordinate system. In the second and third columns the detachment of two auroral features is marked with arrows. In the fourth column the auroral features have reattached into a single arc. A video showing the evolution of the auroral arc in all three cameras, as in Figure 3, is given in Movie S1.

Figure 4 shows the results of the double flow model. The upper row shows the observed metastable emission images, while the bottom row shows the modeled metastable emission images. Each column matches the four times shown in Figure 3. The contours in the top panels indicate the upper 95% brightness in the corresponding lower panels. Comparison of the contours with the background image in the top row shows that the modeled and observed metastable emissions match well. A video showing the comparison between modeled and observed ASK2 images is given in Movie S2.

Velocities estimated from the model are shown in Figure 5, and the corresponding electric fields obtained from these velocities are shown in Figure 6. Values in Figures 5 and 6 represent the magnitudes of the given vectors, while the sign corresponds to the sign of the x-axis component of each vector. On the north side of the auroral arc,
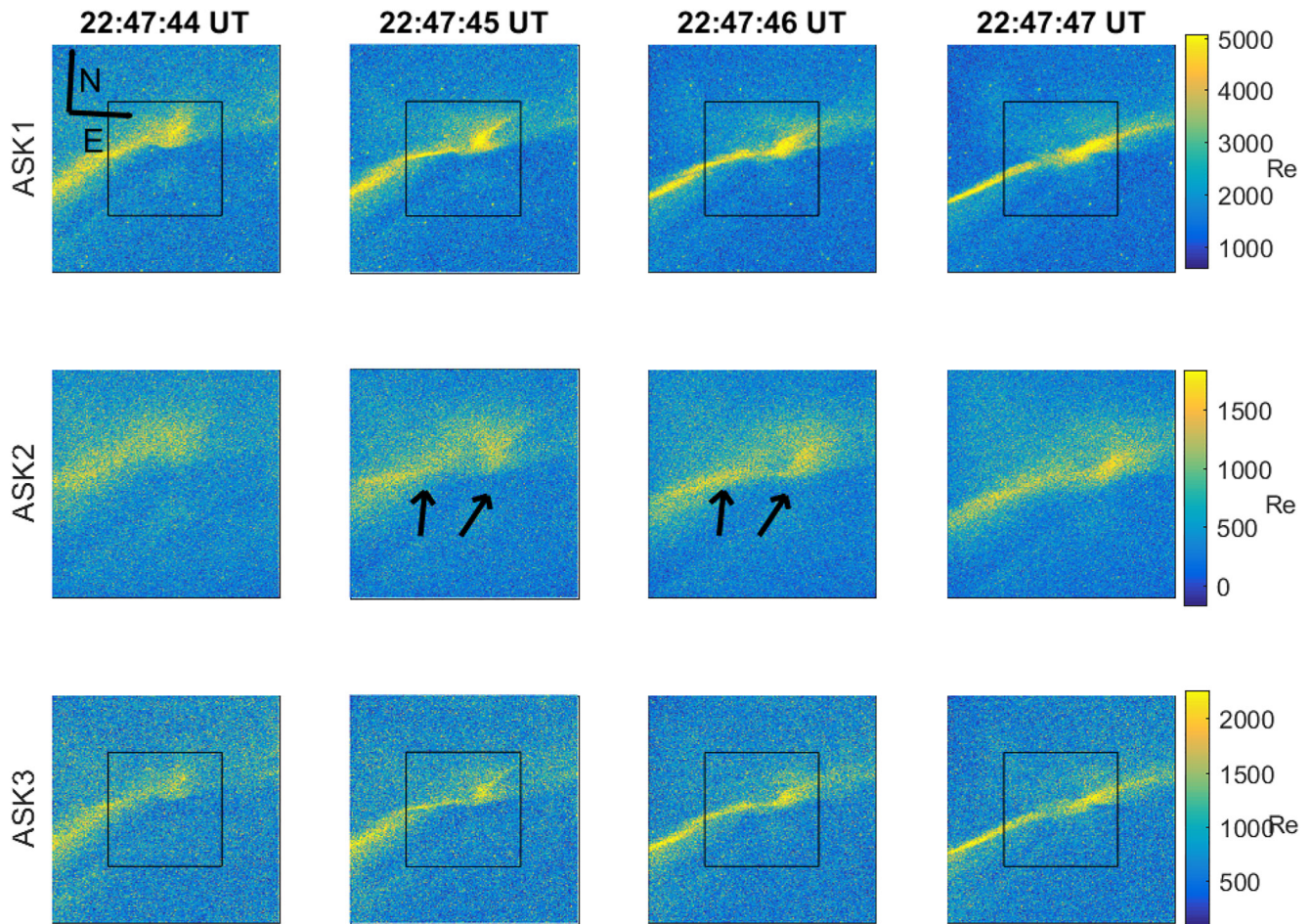
Figure 3. Evolution of the auroral features on 21 December 2014, as seen from the three Auroral Structure and Kinetics instrument (ASK) cameras. Rows indicate the ASK camera number, while columns indicate the times of images labeled above. ASK1 and ASK3 are cameras observing two prompt emissions. ASK2 is the camera observing metastable emission. During this event a telescope was present on ASK2 so the black rectangles on the ASK1 and ASK3 images represent the field of view of ASK2.

electric fields are oriented toward the east direction, while on the south side of the auroral arc, the electric fields are oriented toward the south-east direction. Both sides of the arc show dynamic behavior, with an occasional shear between them. For two instances in our interval, the parallel velocity components had opposite orientation (clear shear), and for two other instances they were exactly the same (no shear), but for most of the event the two velocities had similar orientation but different magnitudes (weak shear).

During the time of the event there were no direct SuperDARN measurements over Svalbard so we used the fitting technique from Ruohoniemi and Greenwald (1996) to obtain a potential map from which we have calculated the background convection velocity. We have chosen to use an 8th order spherical harmonic fit to the convection pattern, which provides a better agreement (not shown) between the 'fitted' vectors which result from the map potential technique, and the 'true' vectors, which combine the measured LOS velocity components with the components of the fitted vectors that are transverse to the LOS direction. Figure 7 shows the potential map with SuperDARN fitted vectors. The location of Svalbard is indicated by a black rectangle. Although there is no scatter over Svalbard at this time, we have plotted a "fitted" vector, which is calculated from the map potential data at the location of the ASK imager, for later comparison. This is the vector plotted with the larger circle, which lies within the black box. The estimated velocity of the fitted flow at this point is 412 m/s.

The neutral wind velocity obtained from the SCANDI instrument was 169.5 m/s mostly in the southern direction. Figures 8 and 9 show all velocities in geographic coordinates from the southern and northern sides of the arc, respectively. Blue vectors are the drift velocities obtained from our model, the red vector is the drift velocity from
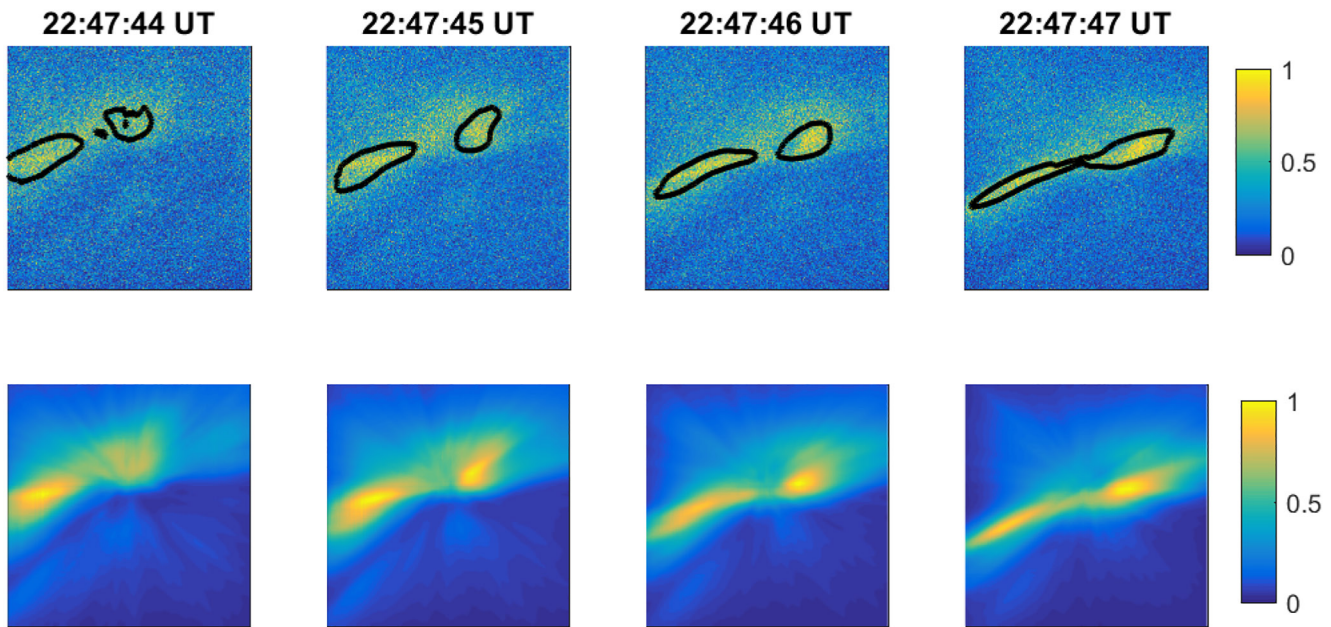
Figure 4. Comparison between modeled and observed images of metastable O^+. Top row shows observed and bottom row modeled images. Contours on the observed images represent the 95% level of the modeled brightness. Time in UT is indicated on top of each column. Images are normalized to the maximum brightness in each image for better comparison.

SuperDARN, and the black vector is the neutral wind. Note, there is a difference in scale on both x and y axes between the two figures.

Figure 10 depicts the estimated Joule heating on both sides of the arc using Equation 4. The black line in Figure 10 represents the height integrated Joule heating using the estimated SuperDARN velocity. Here we can see the differences between Joule heating obtained from local time varying electric fields obtained from our method and Joule heating obtained from more averaged estimated SuperDARN velocity. Table 1 summarizes the results obtained in this paper.
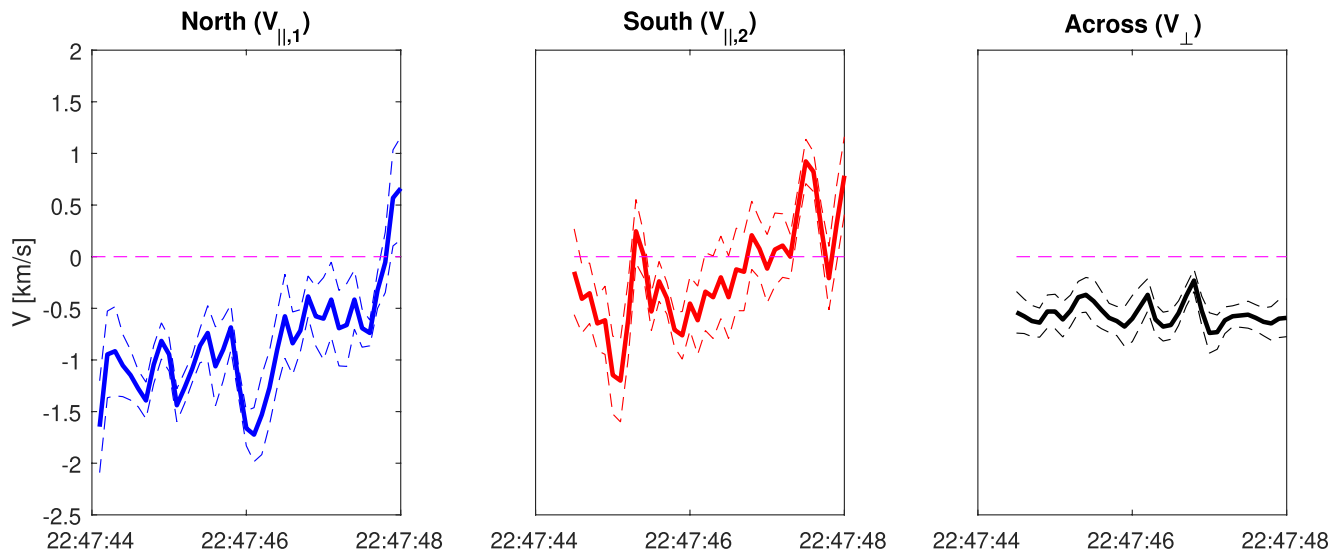
Figure 5. Modeled velocities for each time step. The blue line represents northern parallel velocity, the red line represents southern parallel velocity and the black line represents velocity across the arc. Dashed lines represent standard deviations.
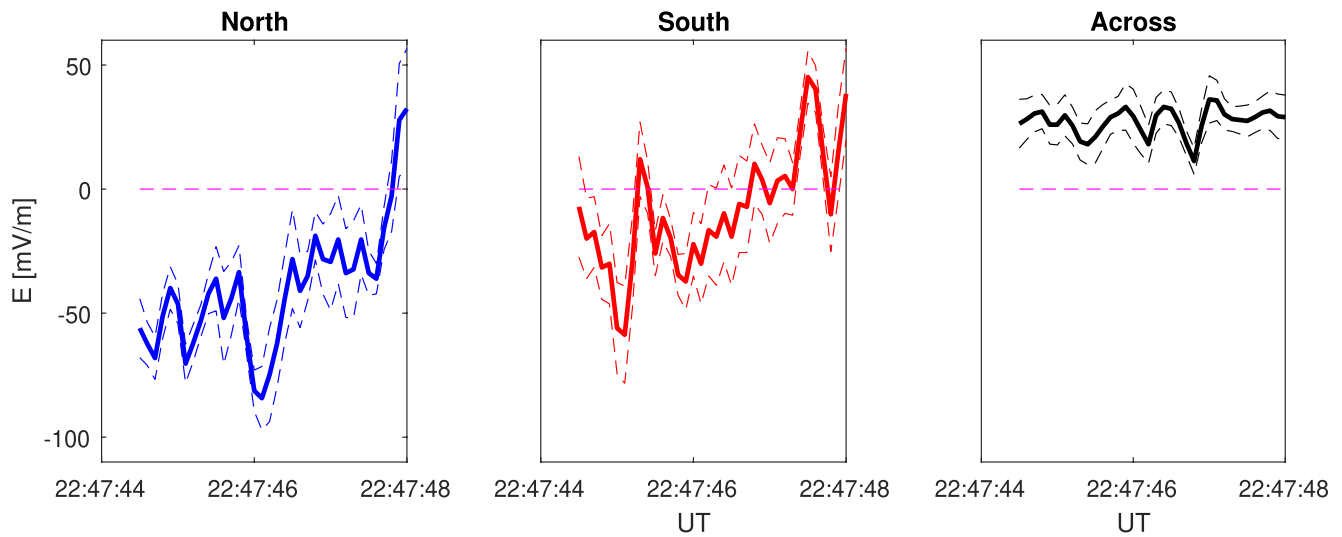
Figure 6. Modeled electric fields for each time step. Line colors are the same as in Figure 5.

5. Discussion

Small scale electric fields have proven crucial in the estimation of Joule heating in the thermosphere. Using the described method we have obtained the electric fields with temporal resolution of 0.1 s and thus have been able to resolve the motion of two auroral features within a single auroral arc. The error analysis presented in supplementary material of this paper suggests somewhat larger standard deviations than that obtained from χ^2 but not as large as the variability shown in Figure 5. We therefore attribute the variability of the ion drift and electric fields presented in this paper to the physical variability of small-scale electric fields. The SuperDARN
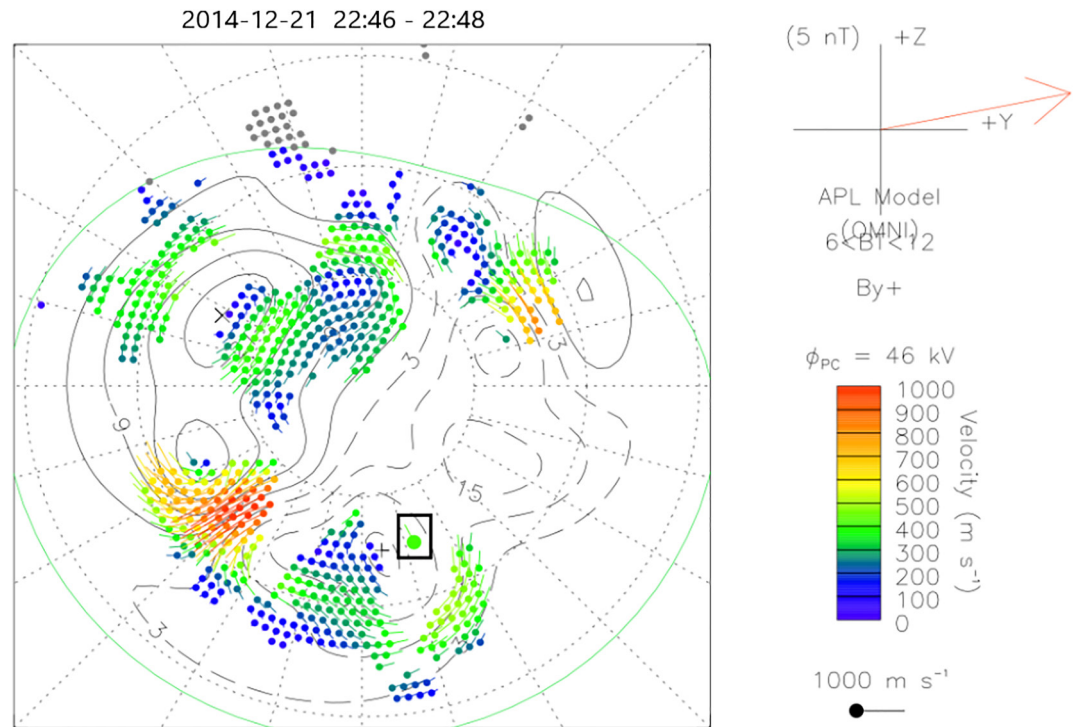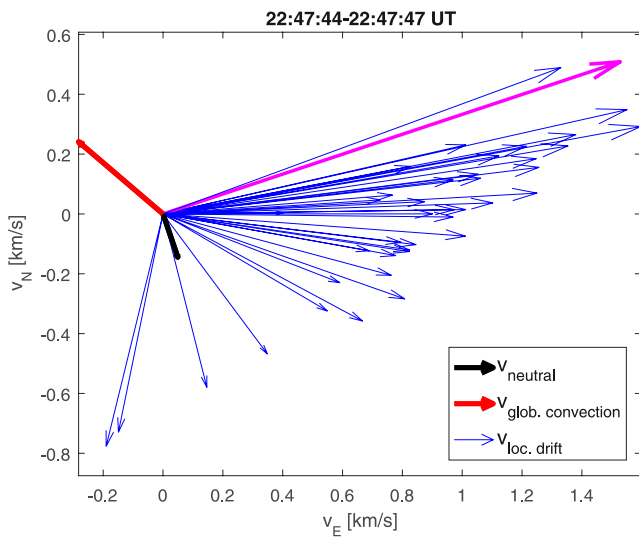

Figure 7. SuperDARN fitted vectors and contours using Ruohoniemi and Baker (1998) statistical model. The Svalbard location is indicated with a black rectangle. Note that this image is magnetic local time coordinate system defined by Sun-Earth line.
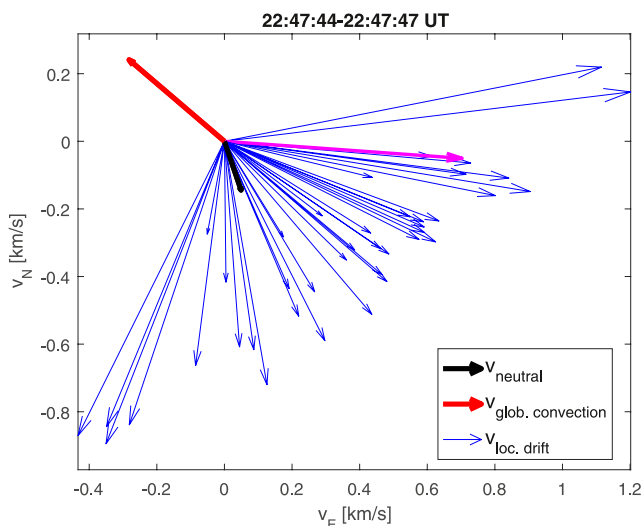
Figure 8. Velocities in the area north of the auroral arc shown in geographic system. Blue vectors represents the drift velocities from optical measurements north of the auroral arc, the red vector represent convection from SuperDARN and the black vector represents the neutral wind obtained from SCANDI. Purple vector is an estimated vector at time 22:47:46.1 used in Figure 11.

potential map in Figure 7 indicates complex ionospheric convection during our event. The potential maps were calculated using the full sweep of the SuperDARN radars which took around 1 min. In the absence of any data over Svalbard, the estimates from SuperDARN are a combination of the effect of the observations to the south and west of Svalbard, and the model potential pattern used for the analysis. As mentioned in Section 2.2, SuperDARN was not designed to make observations on the horizontal spatial scales that are measured by ASK. The individual radars can resolve line-of-sight velocities on scales down to tens of kilometers, which is still much greater than the few kilometres that are resolved by the ASK instrument. Furthermore, the SuperDARN velocity in this study is obtained from the convection map, rather than direct observation from the radar, which additionally smooths out the ion drift variability. The purpose of this study is to highlight the importance of the sub-grid physics, which need to be considered in modeling of auroral regions. The electric fields obtained from optical measurements and modeling are from a 4 s interval, in which an auroral arc passed through the ASK camera view. We are treating electric fields from camera measurements as local electric fields related to the auroral dynamics. Our estimated local drift velocities near the auroral arc (0.3–1.5 km/s) are in agreement with the previous study of Tuttle et al. (2020), who estimated drift velocities around an auroral arc to be varying from 0.4 to 1.2 km/s with peak drift velocity of 2.4 km/s, but their estimate represented a spatial average across the entire field of view. Electric fields are highly variable, varying in both direction and intensity.

The main difference between the results presented in this paper and those in Tuttle et al. (2020) is in the orientation of small-scale electric fields in relation to SuperDARN electric fields. The small-scale electric fields measured by Tuttle et al. (2020) had a good agreement with SuperDARN electric fields, but auroral precipitation in that paper was instantaneous without an additional electromagnetic driver from precipitation. Therefore it is not surprising that the measured drift was in agreement with the convection over Svalbard at the time. In the present work we have continuous precipitation and therefore a sustained potential drop in the ionosphere, which acts as a source of an electric field added to the global convection field. Haerendel (2011) described various mechanisms for the creation of auroral arcs and specifically mentioned that electric fields from most mechanisms (Alfenic arcs, onset arcs, poleward arcs) do not follow the convection pattern. The arc structure in the present study is on a smaller scale than that described by Haerendel (2011), so it is reasonable that the electromagnetic variability is more complex, and not necessarily aligned in direction with the broad convection pattern.

Additionally, Koustov et al. (2019) used the SWARM satellites to measure ion drift and compare it with SuperDARN observations. On average SWARM measured drift velocities that were twice as large as those from SuperDARN, with more discrepancies between the two instruments when SWARM measured large magnitude drifts with values >700 m/s, which is consistent with the results obtained in this study.

Figure 11 shows the drift velocities and electric fields in relation to the auroral arc at 22:47:46.1 UT. The image is from the ASK1 camera (N_2 1PG emission), and vectors are placed at the center of mass of the traced feature brightness. The black dashed line is the position of the separatrix at 132 km which is the average N_2 1PG peak emission height for our event. The average electric fields of both features are oriented in the general direction of the arc movement, but in their time evolution, the electric fields north and south of the separatrix often have different orientations and magnitudes compared with each other.

Figure 9. Velocities in the area south of the auroral arc shown in geographic system. Blue vectors represents drift velocities from optical measurements south of the arc. The rest of the vectors are the same as in Figure 8.
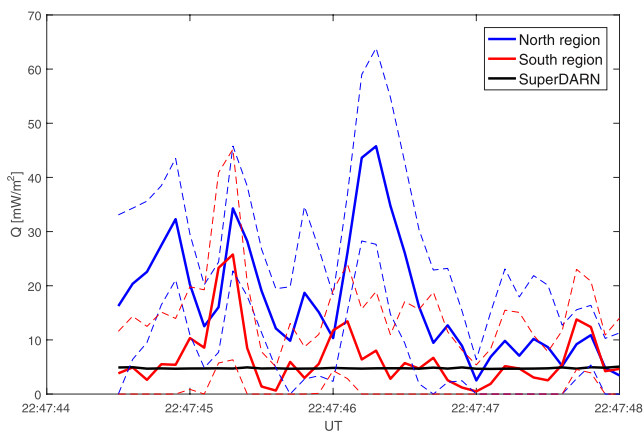
Figure 10. Height integrated Joule heating from both sides of the arc compared with SuperDARN estimates. The red line represents Joule heating south of the auroral arc, the blue line represents Joule heating south of the auroral arc and the black line represents Joule heating obtained from SuperDARN measurements.

By further use of the estimated electric fields we are able to estimate the height integrated Joule heating, while comparing it to a more conventional estimate of the Joule heating based on SuperDARN data. Our Joule heating estimated from small scale electric fields has a peak value of 46 ± 18 mW/m^2 and mean value of 17 ± 11 mW/m^2 for the region north of the auroral arc and a peak value of 26 ± 19 mW/m^2 and mean value of 6 ± 9 mW/m^2 for the region south of the auroral arc. The Joule heating estimated from our optical method shows magnitudes up to 6 times larger on the northern side of the auroral arc and roughly the same values on the southern side of the auroral arc, compared to ones estimated from lower resolution SuperDARN data. The height integrated Joule heating obtained from SuperDARN is 4.8 mW/m^2. Large magnitude and highly dynamic electric fields obtained from our model are the main contributor to the differences in the local and global heating rates. Baker et al. (2004) used SuperDARN data with the Thermosphere, Ionosphere, Mesosphere Energetics and Dynamics spacecraft to obtain heating rates, and estimated peak Joule heating for various geomagnetic conditions over the whole polar cap region. Figure 3 in Baker et al. (2004) shows Joule heating for quiet and moderate geomagnetic conditions similar to those in this paper, which for the general area of Svalbard at the time of our event ($23 - 02$ magnetic local time (MLT), glat = 75–80°) is about 8 mW/m^2.

Weimer (2005) used hybrid field aligned currents and electric potential models to estimate northern hemisphere Joule heating for various clock angle conditions. For clock angle around 90°, similar to one in this paper (73°), Weimer (2005) obtained peak auroral zone Joule heating between 2 and 5 mW/m^2 in the region analyzed in this study ($23 - 02$ MLT, glat = 75–80°). Both global estimates from Baker et al. (2004) and Weimer (2005) are in agreement with more averaged SuperDARN estimates in this study.

The higher local estimates of Joule heating are not surprising. Matsuo and Richmond (2008), analyzed Dynamic Explorer2 spacecraft drift measurements to estimate the effect of sub-grid physics and its underestimate in the electrodynamic general circulation model. The largest electric field variability was shown for the winter hemisphere and northward IMF. Their results show that electric field variability is a significant source of neutral atmosphere heating, with Joule heating increasing 1.5–2.5 times with the inclusion of sub-grid effects. Heelis and Maute (2020) gave an overview of the Earth's ionosphere-thermosphere system and emphasized the importance of small-scale variability in the underestimate of Joule heating. Deng et al. (2009) developed a quantitative empirical model of the high-latitude forcing of the thermosphere with added component of electric field variability, which increased the total Joule heating estimate by more than 100% (comparable with integrated Poynting flux). The conclusions of the above mentioned papers on the effect of variable electric fields on Joule heating are in agreement with those presented here.

The role of the neutral wind and its effect on Joule heating is an important factor. Ions moving in the thermosphere will collide with neutral particles and accelerate them in the direction of the bulk ion drift. In this well known process, the ions that accelerate the neutrals are called 'pick-up' ions (e.g., Tsuda et al., 2007, and others).A typical time scale for the neutral wind to re-orient to the direction of the bulk ion flow is 30 min to 1 hr. The importance of neutral wind in local Joule heating is also highlighted by Kiene et al. (2019) who combined

Table 1
Results of Double-Flow (Marked DF) Model, in Comparison With the Results From Super Dual Auroral Radar Network

	$\overline{E}$ (mVm^{-1})	E_{MAX} (mVm^{-1})	$\overline{\sum Q}$ (mWm^{-2})	$\sum Q_{MAX}$ (mWm^{-2})	En (mJm^{-2})
DF north	53 ± 15	88 ± 16	17 ± 11	46 ± 18	59 ± 22
DF south	36 ± 17	66 ± 21	6 ± 9	26 ± 19	24 ± 18
SuperDARN	20.2		4.8		17.1

Note. $\overline{E}$ is the average value of electric field, while E_{MAX} is the maximum value in the observed interval. Using the same notation $\overline{\sum Q}$ is the average and $\sum Q_{MAX}$ is the maximum value of height integrated Joule heating. En indicates the energy transferred to the atmosphere during our interval, and is obtained by integrating the Joule heating rate over the 4 s duration of the observations.
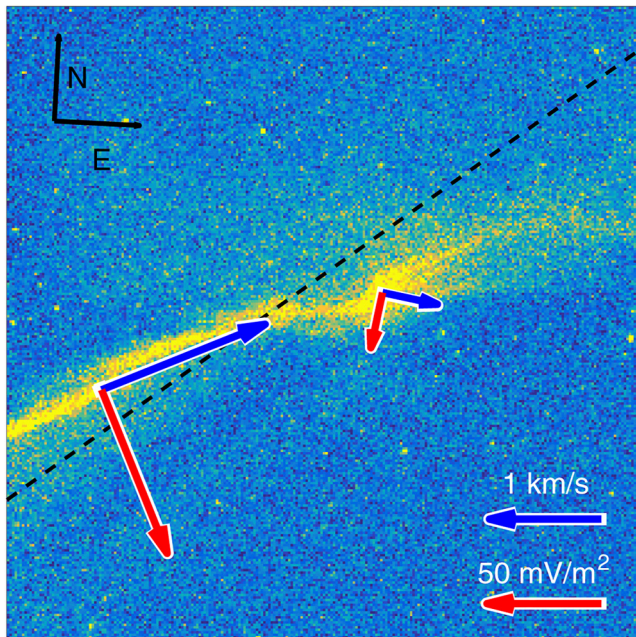
Figure 11. Estimated drifts and electric fields in relation with observed auroral arc. The blue vectors represent drift velocities, the red vectors represent electric field, and black dashed line represent separatrix at 132 km altitude. Vector scales are given in the lower right corner of the panel. Note that image is in camera coordinate system which is rotated by 1.65° in clockwise direction from N-E coordinate system.

SuperDARN and Poker Flat Incoherent Scatter Radar to estimate Joule heating and showed the difference of local hotspots and background Joule heating to be a factor of 10. In their paper Kiene et al. (2019) have also shown that the Joule heating is reduced by a factor of 3 with inclusion of neutral wind once it is oriented in the same direction as the convection velocity. A similar conclusion was given by Billett et al. (2020), who estimated that the Joule heating is reduced to near zero when the neutral wind has the same orientation as the convection velocity. Our results suggest that the importance of small scale electric fields is even greater with inclusion of neutral wind, since the local electric fields can be more intense and are often in a different direction from the bulk electric field caused by the convection. Furthermore, because of the highly dynamic nature of the small-scale electric fields, the neutral wind will not re-orient itself toward the local ion motion but will stay in the same orientation as the bulk flow, resulting in a high intensity local Joule heating (although of short duration). Such significant differences between the local and global estimates indicate the important role of the local Joule heating in the overall dynamics of the thermosphere.

6. Conclusions

Using the ASK instrument and Southampton ion chemistry model we have estimated small-scale electric fields on each side of an auroral arc for an event at 22:47:45 UT on 21 December 2014. The obtained electric fields have subsecond resolution and peak value of 88 ± 16 mVm^{-1} on the northern side of the arc and peak value of 66 ± 21 mVm^{-1} on the southern side of the arc. Using the small scale electric fields and the SCANDI instrument we have calculated the local height integrated Joule heating. Joule heating obtained from small scale electric fields gives much larger values than that obtained from SuperDARN data. We conclude that with high resolution electric fields we can obtain more accurate (larger) estimates of Joule heating which are usually missed with more averaged radar measurements. Therefore, small-scale electric fields play a large role in local, highly intense heating and most likely in overall heating of the ionosphere.

Our optical method for estimating electric fields, and consequently the Joule heating using ASK, has proven to be very valuable in understanding the local heating effects in the vicinity of auroral activity. The method is quite complex, requiring certain conditions to work, such as strong O$^+$ (^{2}P) aurora, clear sky and correct estimation of magnetic zenith. The main goal of further research will be to extend the method to more complicated cases as well as analyzing a wide range of events to reach more general conclusions on local Joule heating and its role in large scale dynamics of the upper atmosphere.

Data Availability Statement

All data used in this research is available at https://doi.org/10.5258/SOTON/D2501.

References

Aikio, A. T., Lakkala, T., Kozlovsky, A., & Williams, P. J. S. (2002). Electric fields and currents of stable drifting auroral arcs in the evening sector. *Journal of Geophysical Research*, *107*(A12), SIA3-1–SIA3-14. https://doi.org/10.1029/2001JA009172

Aruliah, A. L., Griffin, E. M., Aylward, A. D., Ford, E. A. K., Kosch, M. J., Davis, C. J., et al. (2005). First direct evidence of meso-scale variability on ion-neutral dynamics using co-located tristatic FPIs and EISCAT radar in northern Scandinavia. *Annales Geophysicae*, *23*(1), 147–162. https://doi.org/10.5194/angeo-23-147-2005

Aruliah, A. L., Griffin, E. M., Yiu, H.-C. I., McWhirter, I., & Charalambous, A. (2010). SCANDI-an all-sky Doppler imager for studies of thermospheric spatial structure. *Annales Geophysicae*, *28*(2), 549–567. https://doi.org/10.5194/angeo-28-549-2010

Ashrafi, M., Lanchester, B. S., Lummerzheim, D., Ivchenko, N., & Jokiaho, O. (2009). Modelling of N$_2$1P emission rates in aurora using various cross sections for excitation. *Annales Geophysicae*, *27*(6), 2545–2553. https://doi.org/10.5194/angeo-27-2545-2009

Baker, J. B. H., Zhang, Y., Greenwald, R. A., Paxton, L. J., & Morrison, D. (2004). Height-integrated joule and auroral particle heating in the night side high latitude thermosphere. *Geophysical Research Letters*, *31*(9), L09807. https://doi.org/10.1029/2004GL019535

Billett, D. D., Grocott, A., Wild, J. A., Walach, M.-T., & Kosch, M. J. (2018). Diurnal variations in global joule heating morphology and magnitude due to neutral winds. *Journal of Geophysical Research: Space Physics*, *123*(3), 2398–2411. https://doi.org/10.1002/2017JA025141

Billett, D. D., Hosokawa, K., Grocott, A., Wild, J. A., Aruliah, A. L., Ogawa, Y., et al. (2020). Multi-instrument observations of ion-neutral coupling in the dayside cusp. *Geophysical Research Letters*, *47*(4), e2019GL085590. https://doi.org/10.1029/2019GL085590

Chang, T., Torr, D. G., Richards, P. G., & Solomon, S. C. (1993). Reevaluation of the o+(^{2}p) reaction rate coefficients derived from atmosphere explorer c observations. *Journal of Geophysical Research*, *98*(A9), 15589–15597. https://doi.org/10.1029/93JA00957

Chisham, G., Lester, M., Milan, S., Freeman, M., Bristow, W., Grocott, A., et al. (2007). A decade of the super dual auroral radar network (SuperDARN): Scientific achievements, new techniques and future directions. *Surveys in Geophysics*, *28*(1), 33–109. https://doi.org/10.1007/s10712-007-9017-8

Clayton, R., Lynch, K., Zettergren, M., Burleigh, M., Conde, M., Grubbs, G., et al. (2019). Two-dimensional maps of in situ ionospheric plasma flow data near auroral arcs using auroral imagery. *Journal of Geophysical Research: Space Physics*, *124*(4), 3036–3056. https://doi.org/10.1029/2018JA026440

Dahlgren, H., Ivchenko, N., Lanchester, B., Ashrafi, M., Whiter, D., Marklund, G., & Sullivan, J. (2009). First direct optical observations of plasma flows using afterglow of O$^+$ in discrete aurora. *Journal of Atmospheric and Solar-Terrestrial Physics*, *71*(2), 228–238. https://doi.org/10.1016/j.jastp.2008.11.015

Dahlgren, H., Lanchester, B. S., Ivchenko, N., & Whiter, D. K. (2016). Electrodynamics and energy characteristics of aurora at high resolution by optical methods. *Journal of Geophysical Research: Space Physics*, *121*(6), 5966–5974. https://doi.org/10.1002/2016JA022446

Deng, Y., Maute, A., Richmond, A. D., & Roble, R. G. (2009). Impact of electric field variability on joule heating and thermospheric temperature and density. *Geophysical Research Letters*, *36*(8), L08105. https://doi.org/10.1029/2008GL036916

Deng, Y., & Ridley, A. J. (2007). Possible reasons for underestimating joule heating in global models: E field variability, spatial resolution, and vertical velocity. *Journal of Geophysical Research*, *112*(A9), A09308. https://doi.org/10.1029/2006JA012006

Finlay, C. C., Maus, S., Beggan, C. D., Bondar, T. N., Chambodut, A., Chernova, T. A., et al. (2010). International geomagnetic reference field: The eleventh generation. *Geophysical Journal International*, *183*(3), 1216–1230. https://doi.org/10.1111/j.1365-246X.2010.04804.x

Gustavsson, B., Sergienko, T., Rietveld, M. T., Honary, F., Steen, A., Brändström, B. U. E., et al. (2001). First tomographic estimate of volume distribution of HF-pump enhanced airglow emission. *Journal of Geophysical Research*, *106*(A12), 29105–29123. https://doi.org/10.1029/2000JA900167

Haerendel, G. (2011). Six auroral generators: A review. *Journal of Geophysical Research*, *116*(A1), A00K05. https://doi.org/10.1029/2010JA016425

Heelis, R. A., & Maute, A. (2020). Challenges to understanding the earth's ionosphere and thermosphere. *Journal of Geophysical Research: Space Physics*, *125*(7), e2019JA027497. https://doi.org/10.1029/2019JA027497

Kiene, A., Bristow, W. A., Conde, M. G., & Hampton, D. L. (2019). High-resolution local measurements of F region ion temperatures and joule heating rates using SuperDARN and ground-based optics. *Journal of Geophysical Research: Space Physics*, *124*(1), 557–572. https://doi.org/10.1029/2018JA025997

Koustov, A. V., Lavoie, D. B., Kouznetsov, A. F., Burchill, J. K., Knudsen, D. J., & Fiori, R. (2019). A comparison of cross-track ion drift measured by the swarm satellites and plasma convection velocity measured by SuperDARN. *Journal of Geophysical Research: Space Physics*, *124*(6), 4710–4724. https://doi.org/10.1029/2018JA026245

Lanchester, B., & Gustavsson, B. (2012). Imaging of aurora to estimate the energy and flux of electron precipitation. *Auroral Phenomenology and Magnetospheric Processes: Earth and Other Planets*, *197*, 171–182. https://doi.org/10.1029/2011GM001161

Lanchester, B. S., Ashrafi, M., & Ivchenko, N. (2009). Simultaneous imaging of aurora on small scale in oi (777.4 nm) and N$_2$1P to estimate energy and flux of precipitation. *Annales Geophysicae*, *27*(7), 2881–2891. https://doi.org/10.5194/angeo-27-2881-2009

Lanchester, B. S., Kaila, K., & McCrea, I. W. (1996). Relationship between large horizontal electric fields and auroral arc elements. *Journal of Geophysical Research*, *101*(A3), 5075–5084. https://doi.org/10.1029/95JA02055

Lanchester, B. S., Rees, M. H., Lummerzheim, D., Otto, A., Frey, H. U., & Kaila, K. U. (1997). Large fluxes of auroral electrons in filaments of 100 m width. *Journal of Geophysical Research*, *102*(A5), 9741–9748. https://doi.org/10.1029/97JA00231

Marklund, G., Blomberg, L., Fälthammar, C.-G., & Lindqvist, P.-A. (1994). On intense diverging electric fields associated with black aurora. *Geophysical Research Letters*, *21*(17), 1859–1862. https://doi.org/10.1029/94GL00194

Matsuo, T., & Richmond, A. D. (2008). Effects of high-latitude ionospheric electric field variability on global thermospheric joule heating and mechanical energy transfer rate. *Journal of Geophysical Research*, *113*(A7), A07309. https://doi.org/10.1029/2007JA012993

Rees, M. H. (1989). *Physics and chemistry of the upper atmosphere*. Cambridge University Press.

Rees, M. H., Abreu, V. J., & Hays, P. B. (1982). The production efficiency of O$^+$(^{2}p) ions by auroral electron impact ionization. *Journal of Geophysical Research*, *87*(A5), 3612–3616. https://doi.org/10.1029/JA087iA05p03612

Rich, F. J., Gussenhoven, M. S., & Greenspan, M. E. (1987). Using simultaneous particle and field observations on a low altitude satellite to estimate Joule heat energy flow into the high latitude ionosphere. *Annales Geophysicae*, *5*, 527–534.

Robinson, R. M., Vondrak, R. R., Miller, K., Dabbs, T., & Hardy, D. (1987). On calculating ionospheric conductances from the flux and energy of precipitating electrons. *Journal of Geophysical Research*, *92*(A3), 2565–2569. https://doi.org/10.1029/JA092iA03p02565

Ruohoniemi, J. M., & Baker, K. B. (1998). Large-scale imaging of high-latitude convection with super dual auroral radar network HF radar observations. *Journal of Geophysical Research*, *103*(A9), 20797–20811. https://doi.org/10.1029/98JA01288

Ruohoniemi, J. M., & Greenwald, R. A. (1996). Statistical patterns of high-latitude convection obtained from goose bay HF radar observations. *Journal of Geophysical Research*, *101*(A10), 21743–21763. https://doi.org/10.1029/96JA01584

Russell, A. J. B., Wright, A. N., & Streltsov, A. V. (2013). Production of small-scale Alfvén waves by ionospheric depletion, nonlinear magnetosphere-ionosphere coupling and phase mixing. *Journal of Geophysical Research: Space Physics*, *118*(4), 1450–1460. https://doi.org/10.1002/jgra.50168

Rydesäter, P., & Gustavsson, B. (2000). Investigation of smooth basis functions and an approximated projection algorithm for faster tomography. *International Journal of Imaging Systems and Technology*, *11*(6), 347–354. https://doi.org/10.1002/ima.1019

Spry, J., Jokiaho, O., Lanchester, B., & Whiter, D. (2014). Modelling N$_2$1P contamination in auroral O$^+$ emissions. *Journal of Atmospheric and Solar-Terrestrial Physics*, *107*, 8–11. https://doi.org/10.1016/j.jastp.2013.10.013

Stephan, A. W., Meier, R. R., Dymond, K. F., Budzien, S. A., & McCoy, R. P. (2003). Quenching rate coefficients for O$^+$(^{2}P) derived from middle ultraviolet airglow. *Journal of Geophysical Research*, *108*(A1), 1034. https://doi.org/10.1029/2002JA009540

Tsuda, T. T., Nozawa, S., Brekke, A., Ogawa, Y., Motoba, T., Roble, R., & Fujii, R. (2007). An ion drag contribution to the lower thermospheric wind in the summer polar region. *Journal of Geophysical Research*, *112*(A6), A06319. https://doi.org/10.1029/2006JA011785

Tuttle, S., Gustavsson, B., & Lanchester, B. (2014). Temporal and spatial evolution of auroral electron energy spectra in a region surrounding the magnetic zenith. *Journal of Geophysical Research: Space Physics*, *119*(3), 2318–2327. https://doi.org/10.1002/2013JA019627

Tuttle, S., Lanchester, B., Gustavsson, B., Whiter, D., Ivchenko, N., Fear, R., & Lester, M. (2020). Horizontal electric fields from flow of auroral O$^+$(^{2}P) ions at sub-second temporal resolution. *Annales Geophysicae*, *38*(4), 845–859. https://doi.org/10.5194/angeo-38-845-2020

Weimer, D. R. (2005). Improved ionospheric electrodynamic models and application to calculating joule heating rates. *Journal of Geophysical Research*, *110*(A5), A05306. https://doi.org/10.1029/2004JA010884

Whiter, D. K., Lanchester, B. S., Gustavsson, B., Jallo, N. I. B., Jokiaho, O., Ivchenko, N., & Dahlgren, H. (2014). Relative brightness of the O$^+$(^{2}D-^{2}P) doublets in low-energy aurorae. *The Astrophysical Journal*, *797*(1), 64. https://doi.org/10.1088/0004-637x/797/1/64

Zeippen, C. (1987). Improved radiative transition probabilities for O II forbidden lines. *Astronomy and Astrophysics*, *173*, 410–414.